AGU ADVANCING EARTH AND SPACE SCIENCES

Geophysical Research Letters®

RESEARCH LETTER
10.1029/2025GL118147

Davemaoite Elasticity Reveals Slab-Induced Heterogeneity in the Mantle Transition Zone

Yingxin Yu[1], Xinyue Zhang[1], Dongzhou Zhang[2], Luo Li[1], Zhu Mao[1,3], Ningyu Sun[1], Denglei Wang[1], Jing Li[1], Chaoshuai Zhao[1], Cheng Qian[4], Yingzhan Wei[5], Xinyang Li[5], Yuzhu Wang[6], and Takayuki Ishii[7]

[1]State Key Laboratory of Precision Geodesy, School of Earth and Space Sciences, University of Science and Technology of China, Hefei, China, [2]GeoSoilEnviroCARS, University of Chicago, Argonne, IL, USA, [3]National Key Laboratory of Deep Space Exploration, University of Science and Technology of China, Hefei, China, [4]State Key Laboratory of Geological Processes and Mineral Resources, China University of Geosciences, Wuhan, China, [5]State Key Laboratory of High Pressure and Superhard Materials, College of Physics, Jilin University, Changchun, China, [6]Shanghai Advanced Research Institute, Chinese Academy of Sciences, Shanghai, China, [7]Institute for Planetary Materials, Okayama University, Misasa, Japan

Abstract The observed 2%–7% low-shear velocity (V_S) anomalies near the subducted slab at the bottom mantle transition zone (MTZ) indicate strong lateral heterogeneity, which is commonly attributed to subducted oceanic crust. However, davemaoite, a major constituent of the subducted oceanic crust, has been poorly constrained in its elasticity, hindering accurate velocity modeling and obscuring the origin of these low-velocity features. Here we report single-crystal elasticity of Ti-bearing davemaoite with the composition of Ca$(Si_{0.57}Ti_{0.43})O_3$ under high pressure-temperature and found that Ti incorporation significantly reduces velocities and alters the pressure dependence of the shear modulus. Further velocity modeling demonstrated that subducted crusts with varying Ti content have seismic signatures of 1.7(2)–6.8(5)% low-V_S at the bottom MTZ, consistent with the observed low-V_S structure in the region. These findings highlight the role of slab-derived chemical heterogeneity in generating mantle seismic anomalies and provide new experimental constraints on the structure and dynamics of the deep Earth.

Plain Language Summary The origin of seismic anomalies in Earth's mantle is essential for understanding subduction dynamics and chemical evolution of the deep interior. In particular, seismic observations reveal 2%–7% low-shear wave velocity (V_S) anomalies surrounding the subducted slabs at the bottom mantle transition zone (MTZ), indicating strong lateral heterogeneity. These anomalies are commonly attributed to subducted oceanic crusts, which differ compositionally from the normal mantle and is enriched in incompatible elements. A key to understanding these anomalies lies in constraining the elasticity of constituent of minerals in the subducted oceanic crust. However, cubic davemaoite, a key mineral in subducted oceanic crust, has long evaded experimental characterization due to its unquenchable nature. Here we report single-crystal elasticity of Ti-bearing davemaoite under deep mantle conditions, revealing that Ti significantly reduces seismic velocities. Our velocity models show that compositional heterogeneity in subducted slabs can explain the low-velocity anomalies observed at the bottom MTZ. These findings provide a crucial link between deep subduction processes, mantle structure, and seismic observations, offering new insights into Earth's interior dynamics.

Key Points:

- Single-crystal elasticity of Ti-bearing davemaoite is measured at high pressure and temperature conditions
- Our velocity modeling reveals that subducted oceanic crust with varying Ti content generates 1.7%–6.8% V_s reductions at the bottom mantle transition zone
- Ti critically controls both the elasticity and phase stability of davemaoite and influences the seismic responses in the deep mantle

Supporting Information:

Supporting Information may be found in the online version of this article.

Correspondence to:

Z. Mao and T. Ishii,
zhumao@ustc.edu.cn;
takayuki.ishii@okayama-u.ac.jp

Citation:

Yu, Y., Zhang, X., Zhang, D., Li, L., Mao, Z., Sun, N., et al. (2026). Davemaoite elasticity reveals slab-induced heterogeneity in the mantle transition zone. *Geophysical Research Letters*, *53*, e2025GL118147. https://doi.org/10.1029/2025GL118147

Received 17 JUL 2025
Accepted 4 JAN 2026
Corrected 18 APR 2026

This article was corrected on 18 APR 2026. See the end of the full text for details.

Author Contributions:

Conceptualization: Yingxin Yu, Zhu Mao
Data curation: Yingxin Yu, Xinyue Zhang, Luo Li, Ningyu Sun, Denglei Wang, Jing Li, Chaoshuai Zhao, Cheng Qian, Yingzhan Wei, Xinyang Li, Yuzhu Wang, Takayuki Ishii
Formal analysis: Yingxin Yu, Dongzhou Zhang
Funding acquisition: Zhu Mao
Investigation: Yingxin Yu, Dongzhou Zhang, Takayuki Ishii

1. Introduction

The mantle transition zone (MTZ), bounded by the 410-km and 660-km seismic discontinuities, serves as a key layer regulating the transfer of materials and heat between the upper and lower mantle (Goes et al., 2022). Seismic studies have revealed widespread low shear wave velocity (V_S) anomalies with 2%–7.4% reductions surrounding the stagnant slabs at the bottom MTZ in South Africa, Japan Sea, Northeastern China, and Northern America, pointing to significant lateral heterogeneity in composition (Jasbinsek & Dueker, 2007; Y. Shen & Blum, 2003; Tauzin et al., 2017, 2018; Wang et al., 2020).

Water-induced partial melting has commonly been invoked to explain the low-V_S anomalies in the mantle (Hirschmann, 2006; Ohtani, 2020). However, the buoyant, low-viscosity, and highly mobile properties of hydrous melts generated in the MTZ are unfavorable for their long-term preservation, thus making them unlikely to induce

Methodology: Yingxin Yu, Xinyue Zhang, Dongzhou Zhang, Luo Li, Zhu Mao, Ningyu Sun, Denglei Wang, Jing Li, Chaoshuai Zhao
Project administration: Zhu Mao
Supervision: Zhu Mao
Validation: Dongzhou Zhang
Visualization: Yingxin Yu
Writing – original draft: Yingxin Yu, Zhu Mao
Writing – review & editing: Yingxin Yu, Dongzhou Zhang, Zhu Mao, Takayuki Ishii

this heterogeneity (Drewitt et al., 2022). Another key contributor to this heterogeneity is the subducted oceanic crust, which differs markedly in composition from the normal mantle and is enriched in incompatible elements, such as K and Ti (Hirose & Fei, 2002; Irifune et al., 1994; Irifune & Ringwood, 1993; Ishii et al., 2011, 2018; Ricolleau et al., 2010). In particular, davemaoite exsolves from majoritic garnet below ~550-km depth, constituting up to 22–29 vol.% of subducted crustal materials and acting as a major host of incompatible elements (Irifune & Ringwood, 1993; Ishii et al., 2019, 2022; Saikia et al., 2008; Tschauner et al., 2021). However, persistent discrepancies in the reported elastic properties of davemaoite have impeded accurate modeling of the seismic velocity structure of the subducted crust (Gréaux et al., 2019; Kawai & Tsuchiya, 2015; Thomson et al., 2019; Zhang et al., 2025). Resolving this uncertainty is critical to deciphering the origin of low-*Vs* anomalies and their implications for slab dynamics and mantle convection.

A fundamental challenge stems from the metastability of cubic davemaoite: It undergoes spontaneous amorphization or transforms into a tetragonal polymorph upon decompression (Gréaux et al., 2019; Liu & Ringwood, 1975; Mao et al., 1989; Thomson et al., 2019). Although recent high pressure-temperature (P-T) studies on polycrystalline davemaoite provided constraints, their results differ by up to 10% in V_S (Gréaux et al., 2019; Thomson et al., 2019). Besides, theoretical calculation results are inconsistent with either of them, with overprediction of shear moduli by 17%, potentially due to strong anharmonic effects (Kawai & Tsuchiya, 2015; Stixrude et al., 2007; Zhang et al., 2025). More importantly, diamond inclusions originating from the MTZ frequently contain davemaoite enriched in titanium as $CaTiO_3$ component up to 50 mol.%, indicating substantial Ti incorporation in deep-mantle davemaoite assemblages (Brenker et al., 2005; Tappert et al., 2005; Walter et al., 2008). The incorporation of Ti could stabilize tetragonal phases at greater depths, influence the strength of davemaoite, and reduce both the adiabatic bulk (K_S) and shear modulus (G) of davemaoite at ambient conditions (Fischer et al., 1993; Immoor et al., 2022; Liebermann et al., 1977; Sinelnikov et al., 1998; Stixrude et al., 2007; Thomson et al., 2019). Despite its geochemical prevalence, the absence of high P-T elasticity data for Ti-bearing davemaoite leaves a critical gap in linking slab-derived chemical heterogeneities to seismically observable features.

Here, we present the high P-T measurements of single-crystal elasticity for cubic davemaoite [$Ca(Si_{0.57}Ti_{0.43})O_3$]. We show that Ti incorporation not only lowers sound velocities but also modifies the pressure dependence of davemaoite. Forward modeling demonstrates that subducted oceanic crust with varying Ti contents can cause a substantial reduction in the V_S at the bottom MTZ, reconciling chemical heterogeneity with seismic observations. These results provide experimental evidence that incompatible element enrichment in subducted crustal components exerts a crucial control on seismic heterogeneity in the MTZ, offering a new framework for interpreting the composition and dynamics of deep Earth structures.

2. Experiments

2.1. Sample Characterization

The single-crystal Ti-bearing davemaoite used in this study was synthesized at 20 GPa and 2,100 K for 3 hr using a 5,000-ton Kawai-type multi-anvil apparatus at the Institute for Planetary Materials, Okayama University (run# 5K3834). The starting material was prepared by mixing $CaTiO_3$ and natural suolunite ($Ca_2H_2Si_2O_7{\cdot}H_2O$) powder in a molar ratio of 4:3. The $CaTiO_3$ powder was synthesized by mixing $CaCO_3$ and TiO_2 powder in a molar ratio of 1:1 and heating to 1,673 K for 24 hr in a furnace. A cylindrical $LaCrO_3$ heater with two lids was put in the center of a 5-wt% Cr_2O_3-doped MgO octahedral pressure medium with 10-mm edge-length. The powdered starting material was packed in a welded Pt capsule and placed inside the heater. The Pt capsule was insulated from the heater with a MgO capsule. Sample temperature was monitored using a D-type thermocouple at the center part of the capsule surface with no correction for the pressure effect on the electromotive force of the thermocouple. Sample pressure was calibrated against press load using forsterite-wadsleyite and wadsleyite-ringwoodite transitions in Mg_2SiO_4 and akimotoite-bridgmanite transition in $MgSiO_3$ at 1600°C (Chanyshev et al., 2022; Inoue et al., 2006; Morishima et al., 1994).

Single-crystal X-ray diffraction (XRD) has been performed to determine the structure of the synthesized samples at ambient conditions at the State Key Laboratory of Geological Processes and Mineral Resources, China University of Geosciences, Wuhan (Figures S1–S3 in Supporting Information S1). The chemical composition of the synthesized samples was determined by the electron probe microanalyzer (EPMA) in the State Key Laboratory of Lithospheric and Environmental Coevolution, University of Science and Technology of China (USTC) (Table S2

in Supporting Information S1). Diopside was chosen as the standard material for Ca and Si, while rutile served as standard material for Ti. The water content of the recovered samples was characterized by the micro-Fourier Transform Infrared (FTIR) spectrometer in the Infrared Spectroscopy and Microspectroscopy Endstation (BL01B) in the National Synchrotron Radiation Laboratory (NSRL), showing that no water is incorporated into Ti-bearing davemaoite (Figure S4 in Supporting Information S1). We thus obtained the chemical formula of Ca $Si_{0.57}Ti_{0.43}O_3$.

2.2. High P-T Brillouin Scattering Measurements

High P-T Brillouin scattering measurements were performed at the High Pressure and Temperature Mineral Physics Laboratory at USTC up to 17.2 GPa and 700 K. Membrane-driven diamond anvil cells (DACs) were used to generate high P-T conditions. The double-side polished sample platelet of ~90 μm in diameter and ~20 μm in thickness was loaded into each sample chamber DACs equipped with a pair of 500-μm culet diamonds. The sample platelets with the crystallographic orientations of (0.83,−0.50,0.25) and (−0.16,0.18,0.97) determined by Rigaku single-crystal diffraction instrument were used for the measurements under high P and 300 K and high P-T conditions, respectively. 250-μm thick Re foil was pre-indented to ~50 μm in thickness, and a hole with a diameter of 250 μm was drilled to serve as the sample chamber. Ar was used as the pressure-transmitting medium. Ruby was placed next to the sample platelet and used as the pressure calibrant for the experiments under high pressure and 300 K (Datchi et al., 2007).

High P-T experiments were conducted using BX90 DACs (Kantor et al., 2012). High temperature was generated by platinum-rhodium alloy resistive heaters. Temperature was determined by a K-type thermocouple attached to the diamond surface ~500 μm away from the diamond culet. The uncertainty of the temperature measurements in our BX90 DACs was within ±5 K (Sinogeikin et al., 2006). Ruby and Sm^{2+}: SrB_4O_7, placed next to the samples, served as the pressure calibrant during high P-T experiments (Datchi et al., 2007). At 500 K, the difference in pressure determined by Ruby and Sm^{2+}: SrB_4O_7 is less than 0.2 GPa at the investigated pressure range. Due to the overlap of R_1 and R_2 lines of ruby above 600 K, the pressure is only determined by Sm^{2+}: SrB_4O_7 for the experiments at 700 K.

Brillouin scattering system at the High Pressure and Temperature Mineral Physics Laboratory at the USTC was in a symmetric forward-scattering geometry with an external scattering angle of 49.3° for the measurements (Speziale et al., 2014; Whitfield et al., 1976) (Figure S5 in Supporting Information S1). The laser used to excite the signal has a wavelength of 532 nm. The acoustic velocities of Ti-bearing davemaoite were derived by our measured Brillouin frequency shift as follows:

$$v = \frac{\Delta \upsilon_B \lambda_0}{2 \sin(\theta/2)} \tag{1}$$

where v is the acoustic velocity, $\Delta\upsilon_B$ is the measured Brillouin frequency shift, λ_0 is the laser wavelength, and θ is the external scattering angle. Due to the pseudo-cubic structure of Ti-bearing davemaoite, there are three independent elastic moduli that need to be constrained. Thus, we collected Brillouin spectra by varying the azimuthal angles with an interval of 10° over a range of 180° for each P-T condition (Figure S6 in Supporting Information S1).

2.3. High P-T Single-Crystal X-Ray Diffraction

Single-crystal XRD experiments under high P-T conditions were performed at BL17 UM, Shanghai Synchrotron Radiation Facility (SSRF). The wavelength of the X-ray is 0.4834 Å. The gasket, pressure medium, heater, and thermocouple are the same as those of high P-T Brillouin Scattering measurements. One piece of Au foil placed next to the sample platelets served as the pressure calibrant (Fei et al., 2007). A ruby sphere was also loaded into the sample chamber to determine the pressure during gas loading. We collected the XRD data along the isothermal compression at 300 K, 500 K, and 700 K with an interval of 1–2 GPa, respectively. At each pressure, the sample stage was rotated ±20° along its vertical axis to detect as many diffraction spots as possible. The obtained unit-cell parameters are listed in Table S3 in Supporting Information S1, and the equation of state (EoS) data are shown in Figure S7 in Supporting Information S1. The derived EoS parameters are also summarized in Table S7 in Supporting Information S1.

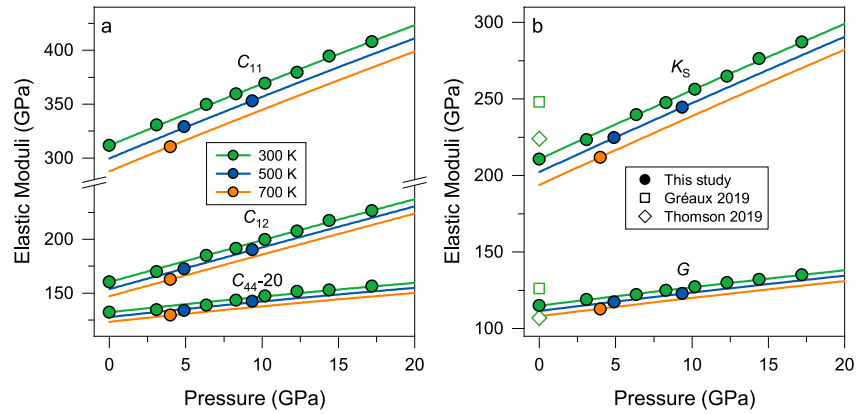

Figure 1. Elastic moduli of Ti-bearing davemaoite under simultaneously high pressure-temperature conditions. (a) C_{11}, C_{12}, and C_{44}; (b) K_S and G. Solid circles: experimental data; solid lines: fitting results. Green: 300 K; blue: 500 K; orange: 700 K. Error bars smaller than the symbols are not shown.

3. Results and Discussions

3.1. Cubic Single-Crystal Davemaoite

Previous studies indicated that Ti-bearing davemaoite might adopt a cubic structure with a space group of $Fm\bar{3}m$ or distort to a low-symmetry structure, based on powder diffraction patterns (Kubo et al., 1997; Leinenweber et al., 1997; Thomson et al., 2019, 2025). However, our single-crystal diffraction pattern suggested that the structure of the sample is best refined by a $Fm\bar{3}c$ space group with a lattice parameter $a = 7.3785(4)$ Å (Data sets S1 and S2, https://doi.org/10.5281/zenodo.18211476). We also attempted the refinements using $Fm\bar{3}m$, $I4/mcm$, and $Pnma$ space group (Data sets S3–S8, https://doi.org/10.5281/zenodo.18211476). However, the refinement with $Fm\bar{3}m$, $I4/mcm$, and $Pnma$ yielded an $R1$ value of 0.0536(45), 0.0767(113), and 0.0911(229), respectively, higher than that of 0.0470(36) obtained for the $Fm\bar{3}c$ structure (Table S1 in Supporting Information S1). We thus believe that the space group of $Fm\bar{3}c$ provides a more appropriate description of the structure of our synthesized sample. Compared to the previously proposed $Fm\bar{3}m$ space group, our determined structure exhibits local distortions induced by the competing chemical bonding requirements of Ti and Si ions that share the same crystallographic sites. More detailed comparisons between these structures have been described in Text S1 in Supporting Information S1.

3.2. Single-Crystal Elasticity of Cubic Davemaoite

We determined single-crystal elasticity and density of Ti-bearing davemaoite with the composition of Ca$(Si_{0.57}Ti_{0.43})O_3$ up to 17.2 GPa and 700 K in externally-heated DACs using Brillouin scattering and synchrotron XRD (Tables S3 and S4 in Supporting Information S1). Our single-crystal sample adopts a pseudo-cubic structure with the space group of $Fm\bar{3}c$, allowing its elastic tensor to be fully described by three independent elastic moduli (C_{11}, C_{12}, and C_{44}). The single-crystal elastic moduli were derived by fitting the measured acoustic velocities at various azimuthal angles using the Christoffel equation (Figure 1 and Table S4 in Supporting Information S1). At ambient conditions, single-crystal elasticity of our Ti-bearing davemaoite is $C_{11} = 312(1)$, $C_{12} = 160(1)$, and $C_{44} = 152(1)$. Using these moduli, we further derived the pressure and temperature derivative of each C_{ij} using the third-order finite strain equation (Table S5 in Supporting Information S1). We also calculated the adiabatic bulk (K_S) and shear moduli (G) of cubic Ti-bearing davemaoite at each P-T condition using the Voigt-Reuss-Hill average and derived their pressure and temperature derivatives by the third-order finite strain equation (Figure 1). At ambient conditions, the derived K_{S0} and G_0 are 211(1) and 115(1), respectively. The pressure derivatives, K_{S0}' and G_0', are 4.25(5) and 1.25(3), respectively, while their temperature derivatives dK_S/dT and dG/dT are −0.042(3) and −0.017(3). We have explicitly considered the effect of the limited high P-T data on the temperature derivatives of the bulk and shear moduli. As a result, the uncertainties in the temperature dependence of K_S and G are slightly larger than those reported for endmember davemaoite in Gréaux et al. (2019), yet remain sufficiently small to provide reliable constraints on their thermal behavior.

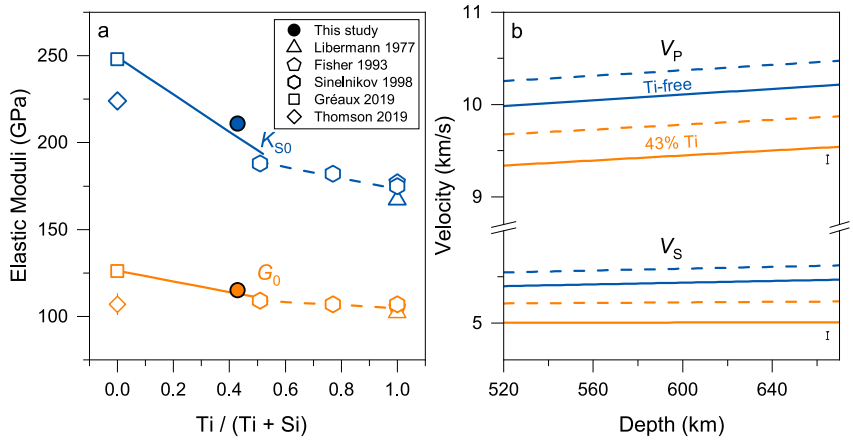

Figure 2. Elasticity and sound velocity of davemaoite with varying Ti content. (a) The effect of Ti content on K_{S0} and G_0. Solid circles: this study; open triangles: Liebermann et al. (1977); open pentagons: Fischer et al. (1993); open hexagons: Sinelnikov et al. (1998); open squares: Gréaux et al. (2019); open diamond: Thomson et al. (2019). Solid lines and dashed lines: fitting results. Error bars smaller than the symbols are not shown. (b) Velocities for Ti-free and Ti-bearing davemoaite. Blue: Ti-free davemaoite; orange: davemaoite with 43% Ti. Solid lines: velocity along a normal mantle geotherm (Brown & Shankland, 1981); dashed lines: velocity along a slab geotherm 500-K colder than the normal mantle.

3.3. Effect of Titanium on the Elasticity of Cubic Davemaoite

Our results together with literature data reveal that the incorporation of Ti into davemaoite leads to a significant decrease in both K_{S0} and G_0, and this reduction is more pronounced for cubic davemaoite with Ti content less than 0.5 [Ti/(Ti + Si)] (Figure 2 and Table S6 in Supporting Information S1) (Fischer et al., 1993; Gréaux et al., 2019; Liebermann et al., 1977; Sinelnikov et al., 1998). Specifically, the addition of 10% Ti results in a decrease of 1.07 (8) GPa in K_{S0} and 0.31(5) GPa in G_0 for cubic davemaoite. When Ti content exceeds 0.5, the incorporation of Ti has minimal impact on G_0, while K_{S0} only decreases by 0.32(5) GPa for the addition of 10% Ti. The role of Ti incorporation in reducing K_{S0} is also supported by the K_{T0} derived from our single-crystal XRD data, which is also smaller than that of endmember davemaoite (Table S7 in Supporting Information S1). Meanwhile, the K_S exhibits P-T behavior similar to that of endmember davemaoite, while the G shows weaker pressure dependence but comparable temperature response. Elevating the temperature of 100 K leads to a decrease of ~1.7 GPa in G, compared to a reduction of 1.5–3.0 GPa for endmember davemaoite (Gréaux et al., 2019; Thomson et al., 2019).

To further explore the effect of Ti incorporation on the elasticity of davemaoite, we modeled the sound velocity of Ti-bearing and endmember davemaoite along different mantle geotherms (Figure 2) (Brown & Shankland, 1981). At 520-km depth, the compressional-wave velocity (V_P) and V_S of Ti-bearing davemaoite along normal mantle geotherms are 6.7(3)% and 7.6(4)% lower than endmember davemaoite, respectively (Gréaux et al., 2019). The difference in V_S between endmember and our Ti-bearing davemaoite increases to 8.8(4)% at 660-km depth due to the smaller pressure derivative of G of Ti-bearing davemaoite. Decreasing temperature slightly reduces the velocity difference between endmember and Ti-bearing davemaoite. For example, along the slab geotherm 500-K colder than the normal mantle, the differences in V_P and V_S between endmember and Ti-bearing davemaoite are 5.8(3)% and 6.2–7.2(4)% at depths of 520–660 km, respectively. These results collectively demonstrate that variations in Ti content can significantly modulate the seismic properties of davemaoite in the lower MTZ. Even modest Ti incorporation leads to pronounced reductions in both V_P and V_S, with the magnitude of softening increasing with depth along the mantle geotherm.

Using our derived single-crystal elasticity, we further calculated the maximum azimuthal compressional anisotropy, $A_P[(V_{P,\max}-V_{P,\min})/V_{P,\text{average}}]$, and shear-wave splitting, $A_S^{PO}[(V_{S2}-V_{S1})_{\max}/V_{S,\text{average}}]$, of Ti-bearing davemaoite along the mantle geotherm, and then compared them with those of major minerals in the bottom MTZ (Figure S8 in Supporting Information S1). Because no experimental single-crystal elasticity is available for endmember davemaoite, its seismic anisotropy relies on two theoretical calculations (Kawai & Tsuchiya, 2015; Zhang et al., 2025). Zhang et al. (2025) suggests a much stronger anisotropy than Kawai and Tsuchiya (2015). Our Ti-bearing davemaoite lies between these two endmember predictions, making it difficult to draw a definitive conclusion about the effect of Ti on davemaoite anisotropy. Despite this uncertainty, both endmember

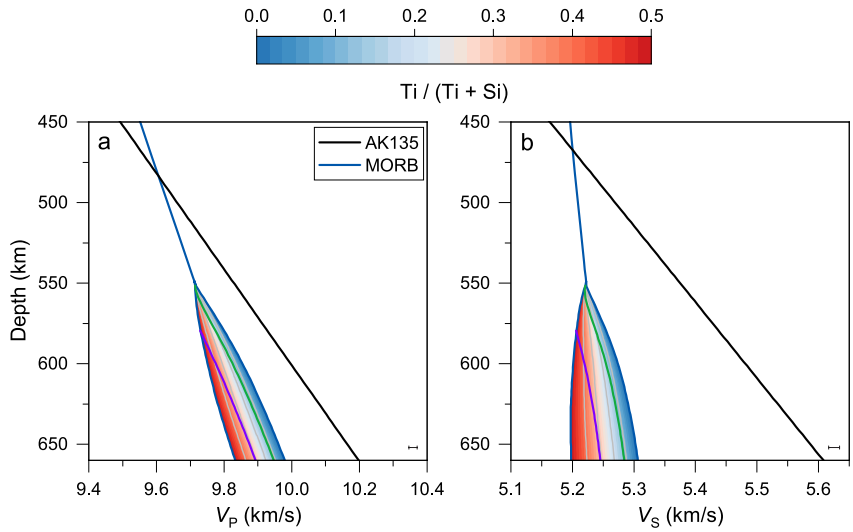

Figure 3. Velocity profiles of the subducted oceanic crust with the variation of Ti content in davemaoite within the mantle transition zone. (a) V_P; (b) V_S. Blue lines: MORB; black lines: 1D seismic reference model AK135 (Kennett et al., 1995); green lines: MORB with 1.7 wt.% TiO_2 in bulk composition; purple lines: MORB with 4.4 wt.% TiO_2 in bulk composition. The contour represents the velocity profiles with a constant Ti content in davemaoite. Geotherm: Brown and Shankland (1981).

and Ti-bearing davemaoite exhibit A_P and A_S^{PO} values that are lower than those of stishovite but higher than those of ringwoodite and majorite in the bottom MTZ. Additionally, our results show that A_P and A_S^{PO} for Ti-bearing davemaoite decrease slightly with depth.

4. Geophysical Implication

The ubiquitous low-V_S anomalies at the bottom MTZ have been attributed to the accumulation of subducted oceanic crusts (Y. Shen & Blum, 2003; X. Shen et al., 2014; Wei et al., 2021). Importantly, our experimental determination of single-crystal elastic moduli of cubic davemaoite at high P-T represents a critical advance, enabling more accurate constraints on the seismic properties of subducted oceanic crust within the MTZ. This breakthrough further reveals that the incorporation of incompatible elements, particularly Ti, can substantially reduce seismic velocities, providing a new framework for reassessing the origins of low-velocity anomalies at these depths. To establish a compositional reference, we first constructed a velocity model for Ti-free subducted oceanic crust along a normal mantle geotherm, which serves as a baseline for evaluating the seismic effects of chemical variations (Figure 3 and see Texts S3 and S4 in Supporting Information S1 for details in modeling) (Brown & Shankland, 1981).

Our modeling revealed that the sound velocity of the subducted oceanic crust is indistinguishable from the 1D seismic reference model AK135 at depths shallower than ~500 km (Kennett et al., 1995). Below this depth, the subducted oceanic crust gradually exhibits a seismic signature with a lower velocity compared to normal mantle, and the difference between them increases with depth. Prior to the exsolution of davemaoite at ~550-km depth, V_P and V_S of the subducted oceanic crust are 1.1(2)% and 2.8(3)% lower than those of normal mantle, respectively (Figure 4). Below ~550 km depths, progressive exsolution of davemaoite alters the velocity gradient, and the contrast between the subducted oceanic crust and normal mantle increases with depth. At 600-km depth, V_P and V_S of the subducted oceanic crust are 1.5(2)% and 3.9(3)% lower than the normal mantle. Once subducted oceanic crust reaches the depths of 660 km, it could be detected as a low-velocity structure with 2.2(3)% lower V_P and 5.6 (4)% lower V_S.

The incorporation of Ti during davemaoite exsolution further complicates the seismic velocity profile of subducted oceanic crust (Figures 3 and 4). Increasing Ti content in davemaoite leads to a pronounced reduction in seismic velocities, thereby enhancing the contrast between the subducted crust and normal mantle. For example, when davemaoite contains 10% Ti, the low velocity anomalies of subducted oceanic crust in V_P and V_S are 2.5 (3)% and 5.9(4)% compared to normal mantle at depths of 660 km. With Ti content up to 50%, the composition

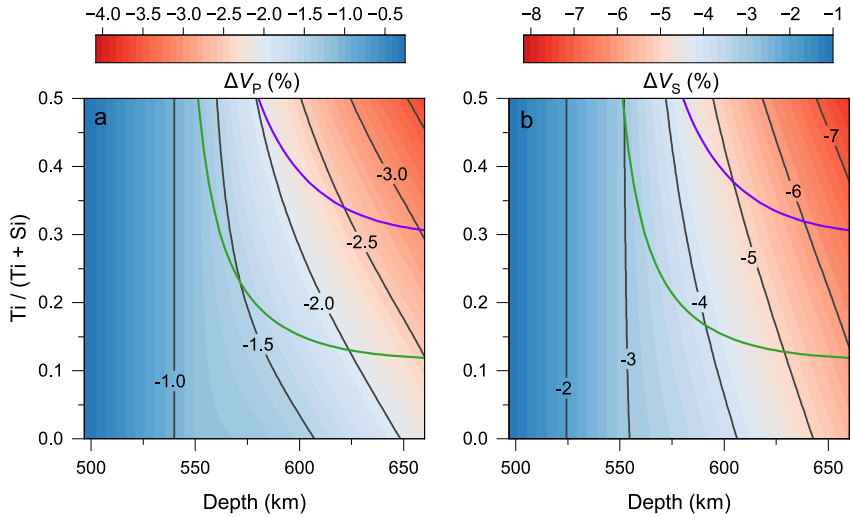

Figure 4. The velocity contrast between MORB and AK135 with varying Ti content in davemaoite at the bottom of the mantle transition zone. (a) Compressional velocity contrast, ΔV_P; (b) Shear velocity contrast, ΔV_S. $\Delta M = 2(M_{\mathrm{MORB}} - M_{\mathrm{AK135}})/(M_{\mathrm{MORB}} + M_{\mathrm{AK135}})$, $M = V_P$ and V_S. Green lines: the Ti content variation in davemaoite for MORB with 1.7 wt.% TiO_2 in bulk composition; purple lines: the Ti content variation in davemaoite for MORB with 4.4 wt.% TiO_2 in bulk composition.

commonly observed in davemaoite inclusions in superdeep diamonds, the velocity anomalies can reach as much as −3.7(3)% and −7.6(5)% in V_P and V_S at 660-km depths (Brenker et al., 2005; Tappert et al., 2005; Walter et al., 2008).

Under realistic mantle conditions, the Ti content in davemaoite is primarily governed by the bulk TiO_2 content of the subducted crust, the partitioning among the coexisting mineral phases, and the extent of the exsolution process (Gale et al., 2013; Gréaux et al., 2018; Hirose & Fei, 2002; Ishii et al., 2019; Litasov & Ohtani, 2005; Ono et al., 2001). In the subducted oceanic crusts with a typical TiO_2 content of 1.7 wt.%, davemaoite composition evolves from $Ca(Si_{0.5}Ti_{0.5})O_3$ to $Ca(Si_{0.9}Ti_{0.1})O_3$ during the exsolution, and the corresponding low-V_P and V_S anomalies at the bottom of MTZ (550–660 km depth) are 1.2(2)–2.5(3)% and 3.0(3)–6.0(5)%, respectively. In regions where TiO_2 concentration reaches the upper bound of 4.4 wt.%, the change in composition of davemaoite from $Ca(Si_{0.5}Ti_{0.5})O_3$ to $Ca(Si_{0.7}Ti_{0.3})O_3$ would enhance the low-velocity anomalies to 2.0(4)–3.1(4)% for V_P at the bottom of MTZ and 4.4(4)–6.8(5)% for V_S (Gale et al., 2013).

Our forward modeling indicates that subducted oceanic crust inevitably exhibits significantly lower seismic velocities than the normal mantle at the bottom MTZ. In particular, for slabs stagnating within the MTZ, the deceleration of slab descent can lead to thickening via buckling, and even segregation of the oceanic crust (Ballmer et al., 2015; Feng et al., 2021; Fukao & Obayashi, 2013; Goes et al., 2017; Immoor et al., 2022). The accumulation of subducted oceanic crust at MTZ depths enhances its seismic detectability as low-velocity anomalies. Even in the absence of Ti, such crustal accumulation produces velocity reductions of 1.7(3)–5.6(4)% in V_S, consistent with seismic observations of low-velocity structures in the Southern Africa, Japan Sea, and Northeastern China regions (Y. Shen & Blum, 2003; Tauzin et al., 2017; Wang et al., 2020). When the subducted oceanic crust contains typical Ti contents of 1.7 wt.%, the accumulated material at the bottom MTZ shows even greater V_S reductions of 3.0(3)–6.0(5)%, matching the larger V_S anomalies observed in the Northeastern China (Gale et al., 2013; Wang et al., 2020). While Ti content in the subducted oceanic crusts reaches up to the upper bound of 4.4 wt.%, the resulting low-V_S anomalies range from 4.4(4)% to 6.8(5)%, thus satisfying the observation beneath the Northern America (Gale et al., 2013; Jasbinsek & Dueker, 2007). These results provide a quantitative explanation for the seismic low-V_S anomalies observed at the bottom MTZ, demonstrating that the presence and composition of oceanic crust, particularly its Ti content, play a key role in shaping deep-mantle seismic structure. More broadly, our findings highlight that deep-mantle seismic anomalies reflect extensive compositional heterogeneity, intimately linked to slab dynamics, mantle convection, and long-term material cycling. The influence of incompatible elements such as Ti on elasticity and phase stability further underscores their critical role in the generation and preservation of chemical heterogeneity within Earth's interior.

Conflict of Interest

The authors declare no conflicts of interest relevant to this study.

Data Availability Statement

The structure file and data generated in this study can be found in the online Supporting information. They can also be downloaded online Yu et al. (2025) (from https://doi.org/10.5281/zenodo.18211476).

Acknowledgments
This work was supported by the National Science Foundation of China (42425202 and 42488101) and National Key R&D Program of China (2023YFF0803200) to Z. M, and JSPS KAKENHI Grants (23K19067 and 24K00735) and JSPS Bilateral Joint Research Projects (JPJSBP120247413) to T. I. This work was partially carried out at the high-pressure synergetic measurement station of Synergic Extreme Condition User Facility. We thank the Shanghai Synchrotron Radiation Facility of BL17UM (31124.02.SSRF.BL17UM) for the assistance on high P-T XRD measurements (proposal: 2024-SSRF-PT-506102, 2025-SSRF-HZ-511166). FTIR data were collected at the Infrared Spectroscopy and Microspectroscopy Endstation (BL01B) in the National Synchrotron Radiation Laboratory (NSRL). We acknowledge H. L for the assistance in FTIR data collection and N. K, T. X, and W. L for the assistance in EPMA measurements.

References

Ballmer, M. D., Schmerr, N. C., Nakagawa, T., & Ritsema, J. (2015). Compositional mantle layering revealed by slab stagnation at ~1,000-km depth. *Science Advances*, *1*(11), e1500815. https://doi.org/10.1126/sciadv.1500815

Brenker, F. E., Vincze, L., Vekemans, B., Nasdala, L., Stachel, T., Vollmer, C., et al. (2005). Detection of a Ca-rich lithology in the Earth's deep (>300 km) convecting mantle. *Earth and Planetary Science Letters*, *236*(3–4), 579–587. https://doi.org/10.1016/j.epsl.2005.05.021

Brown, J. M., & Shankland, T. (1981). Thermodynamic parameters in the Earth as determined from seismic profiles. *Geophysical Journal International*, *66*(3), 579–596. https://doi.org/10.1111/j.1365-246x.1981.tb04891.x

Chanyshev, A., Ishii, T., Bondar, D., Bhat, S., Kim, E. J., Farla, R., et al. (2022). Depressed 660-km discontinuity caused by Akimotoite–Bridgmanite transition. *Nature*, *601*(7891), 69–73. https://doi.org/10.1038/s41586-021-04157-z

Datchi, F., Dewaele, A., Loubeyre, P., Letoullec, R., Le Godec, Y., & Canny, B. (2007). Optical pressure sensors for high-pressure–high-temperature studies in a diamond anvil cell. *High Pressure Research*, *27*(4), 447–463. https://doi.org/10.1080/08957950701659593

Drewitt, J. W., Walter, M. J., Brodholt, J. P., Muir, J. M., & Lord, O. T. (2022). Hydrous silicate melts and the deep mantle H_2O cycle. *Earth and Planetary Science Letters*, *581*, 117408. https://doi.org/10.1016/j.epsl.2022.117408

Fei, Y., Ricolleau, A., Frank, M., Mibe, K., Shen, G., & Prakapenka, V. (2007). Toward an internally consistent pressure scale. *Proceedings of the National Academy of Sciences*, *104*(22), 9182–9186. https://doi.org/10.1073/pnas.0609013104

Feng, J., Yao, H., Wang, Y., Poli, P., & Mao, Z. (2021). Segregated oceanic crust trapped at the bottom mantle transition zone revealed from ambient noise interferometry. *Nature Communications*, *12*(1), 2531. https://doi.org/10.1038/s41467-021-22853-2

Fischer, G. J., Wang, Z., & Karato, S.-i. (1993). Elasticity of $CaTiO_3$, $SrTiO_3$ and $BaTiO_3$ perovskites up to 3.0 Gpa: The effect of crystallographic structure. *Physics and Chemistry of Minerals*, *20*(2), 97–103. https://doi.org/10.1007/bf00207202

Fukao, Y., & Obayashi, M. (2013). Subducted slabs stagnant above, penetrating through, and trapped below the 660 km discontinuity. *Journal of Geophysical Research: Solid Earth*, *118*(11), 5920–5938. https://doi.org/10.1002/2013jb010466

Gale, A., Dalton, C. A., Langmuir, C. H., Su, Y., & Schilling, J. G. (2013). The mean composition of ocean ridge basalts. *Geochemistry, Geophysics, Geosystems*, *14*(3), 489–518. https://doi.org/10.1002/ggge.20038

Goes, S., Agrusta, R., van Hunen, J., & Garel, F. (2017). Subduction-transition zone interaction: A review. *Geosphere*, *13*(3), 644–664. https://doi.org/10.1130/ges01476.1

Goes, S., Yu, C., Ballmer, M. D., Yan, J., & van der Hilst, R. D. (2022). Compositional heterogeneity in the mantle transition zone. *Nature Reviews Earth & Environment*, *3*(8), 533–550. https://doi.org/10.1038/s43017-022-00312-w

Gréaux, S., Irifune, T., Higo, Y., Tange, Y., Arimoto, T., Liu, Z., & Yamada, A. (2019). Sound velocity of $CaSiO_3$ perovskite suggests the presence of basaltic crust in the Earth's lower mantle. *Nature*, *565*(7738), 218–221. https://doi.org/10.1038/s41586-018-0816-5

Gréaux, S., Nishi, M., Tateno, S., Kuwayama, Y., Hirao, N., Kawai, K., et al. (2018). High-pressure phase relation of KREEP basalts: A clue for finding the lost Hadean crust? *Physics of the Earth and Planetary Interiors*, *274*, 184–194. https://doi.org/10.1016/j.pepi.2017.12.004

Hirose, K., & Fei, Y. (2002). Subsolidus and melting phase relations of basaltic composition in the uppermostlower mantle. *Geochimica et Cosmochimica Acta*, *66*(12), 2099–2108. https://doi.org/10.1016/s0016-7037(02)00847-5

Hirschmann, M. M. (2006). Water, melting, and the deep Earth H_2O cycle. *Annual Review of Earth and Planetary Sciences*, *34*(1), 629–653. https://doi.org/10.1146/annurev.earth.34.031405.125211

Immoor, J., Miyagi, L., Liermann, H.-P., Speziale, S., Schulze, K., Buchen, J., et al. (2022). Weak cubic $CaSiO_3$ perovskite in the Earth's mantle. *Nature*, *603*(7900), 276–279. https://doi.org/10.1038/s41586-021-04378-2

Inoue, T., Irifune, T., Higo, Y., Sanehira, T., Sueda, Y., Yamada, A., et al. (2006). The phase boundary between wadsleyite and ringwoodite in Mg_2SiO_4 determined by in situ X-ray diffraction. *Physics and Chemistry of Minerals*, *33*(2), 106–114. https://doi.org/10.1007/s00269-005-0053-y

Irifune, T., & Ringwood, A. (1993). Phase transformations in subducted oceanic crust and buoyancy relationships at depths of 600–800 km in the mantle. *Earth and Planetary Science Letters*, *117*(1–2), 101–110. https://doi.org/10.1016/0012-821x(93)90120-x

Irifune, T., Ringwood, A., & Hibberson, W. (1994). Subduction of continental crust and terrigenous and pelagic sediments: An experimental study. *Earth and Planetary Science Letters*, *126*(4), 351–368. https://doi.org/10.1016/0012-821x(94)90117-1

Ishii, T., Kojitani, H., & Akaogi, M. (2011). Post-spinel transitions in pyrolite and Mg_2SiO_4 and akimotoite–perovskite transition in $MgSiO_3$: Precise comparison by high-pressure high-temperature experiments with multi-sample cell technique. *Earth and Planetary Science Letters*, *309*(3–4), 185–197. https://doi.org/10.1016/j.epsl.2011.06.023

Ishii, T., Kojitani, H., & Akaogi, M. (2018). Phase relations and mineral chemistry in pyrolitic mantle at 1600–2200°C under pressures up to the uppermost lower mantle: Phase transitions around the 660-km discontinuity and dynamics of upwelling hot plumes. *Physics of the Earth and Planetary Interiors*, *274*, 127–137. https://doi.org/10.1016/j.pepi.2017.10.005

Ishii, T., Kojitani, H., & Akaogi, M. (2019). Phase relations of harzburgite and MORB up to the uppermost lower mantle conditions: Precise comparison with pyrolite by multisample cell high-pressure experiments with implication to dynamics of subducted slabs. *Journal of Geophysical Research: Solid Earth*, *124*(4), 3491–3507. https://doi.org/10.1029/2018jb016749

Ishii, T., Miyajima, N., Criniti, G., Hu, Q., Glazyrin, K., & Katsura, T. (2022). High pressure-temperature phase relations of basaltic crust up to mid-mantle conditions. *Earth and Planetary Science Letters*, *584*, 117472. https://doi.org/10.1016/j.epsl.2022.117472

Jasbinsek, J., & Dueker, K. (2007). Ubiquitous low-velocity layer atop the 410-km discontinuity in the northern Rocky Mountains. *Geochemistry, Geophysics, Geosystems*, *8*(10). https://doi.org/10.1029/2007GC001661

Kantor, I., Prakapenka, V., Kantor, A., Dera, P., Kurnosov, A., Sinogeikin, S., et al. (2012). BX90: A new diamond anvil cell design for X-ray diffraction and optical measurements. *Review of Scientific Instruments*, *83*(12), 125102. https://doi.org/10.1063/1.4768541

Kawai, K., & Tsuchiya, T. (2015). Small shear modulus of cubic $CaSiO_3$ perovskite. *Geophysical Research Letters*, *42*(8), 2718–2726. https://doi.org/10.1002/2015gl063446

Kennett, B. L., Engdahl, E., & Buland, R. (1995). Constraints on seismic velocities in the Earth from traveltimes. *Geophysical Journal International*, *122*(1), 108–124. https://doi.org/10.1111/j.1365-246x.1995.tb03540.x

Kubo, A., Suzuki, T., & Akaogi, M. (1997). High pressure phase equilibria in the system $CaTiO_3$-$CaSiO_3$: Stability of perovskite solid solutions. *Physics and Chemistry of Minerals*, *24*(7), 488–494. https://doi.org/10.1007/s002690050063

Leinenweber, K., Grzechnik, A., Voorhees, M., Navrotsky, A., Yao, N., & McMillan, P. F. (1997). Structural variation in $Ca(Ti_xSi_{1-x})O_3$ perovskites (1> x> 0.65) and the ordered phase Ca_2TiSiO_6. *Physics and Chemistry of Minerals*, *24*, 528–534.

Liebermann, R. C., Jones, L. E., & Ringwood, A. (1977). Elasticity of aluminate, titanate, stannate and germanate compounds with the perovskite structure. *Physics of the Earth and Planetary Interiors*, *14*(2), 165–178. https://doi.org/10.1016/0031-9201(77)90152-2

Litasov, K. D., & Ohtani, E. (2005). Phase relations in hydrous MORB at 18–28 GPa: Implications for heterogeneity of the lower mantle. *Physics of the Earth and Planetary Interiors*, *150*(4), 239–263. https://doi.org/10.1016/j.pepi.2004.10.010

Liu, L.-G., & Ringwood, A. (1975). Synthesis of a perovskite-type polymorph of $CaSiO_3$. *Earth and Planetary Science Letters*, *28*(2), 209–211. https://doi.org/10.1016/0012-821x(75)90229-0

Mao, H. K., Chen, L., Hemley, R., Jephcoat, A., Wu, Y., & Bassett, W. (1989). Stability and equation of state of $CaSiO_3$-perovskite to 134 GPa. *Journal of Geophysical Research*, *94*(B12), 17889–17894. https://doi.org/10.1029/jb094ib12p17889

Morishima, H., Kato, T., Suto, M., Ohtani, E., Urakawa, S., Utsumi, W., et al. (1994). The phase boundary between α-and β-Mg_2SiO_4 determined by in situ X-ray observation. *Science*, *265*(5176), 1202–1203. https://doi.org/10.1126/science.265.5176.1202

Ohtani, E. (2020). The role of water in Earth's mantle. *National Science Review*, *7*(1), 224–232. https://doi.org/10.1093/nsr/nwz071

Ono, S., Ito, E., & Katsura, T. (2001). Mineralogy of subducted basaltic crust (MORB) from 25 to 37 GPa, and chemical heterogeneity of the lower mantle. *Earth and Planetary Science Letters*, *190*(1–2), 57–63. https://doi.org/10.1016/s0012-821x(01)00375-2

Ricolleau, A., Perrillat, J. p., Fiquet, G., Daniel, I., Matas, J., Addad, A., et al. (2010). Phase relations and equation of state of a natural MORB: Implications for the density profile of subducted oceanic crust in the Earth's lower mantle. *Journal of Geophysical Research*, *115*(B8). https://doi.org/10.1029/2009jb006709

Saikia, A., Frost, D. J., & Rubie, D. C. (2008). Splitting of the 520-kilometer seismic discontinuity and chemical heterogeneity in the mantle. *Science*, *319*(5869), 1515–1518. https://doi.org/10.1126/science.1152818

Shen, X., Yuan, X., & Li, X. (2014). A ubiquitous low-velocity layer at the base of the mantle transition zone. *Geophysical Research Letters*, *41*(3), 836–842. https://doi.org/10.1002/2013gl058918

Shen, Y., & Blum, J. (2003). Seismic evidence for accumulated oceanic crust above the 660-km discontinuity beneath southern Africa. *Geophysical Research Letters*, *30*(18). https://doi.org/10.1029/2003gl017991

Sinelnikov, Y. D., Chen, G., & Liebermann, R. C. (1998). Elasticity of $CaTiO_3$–$CaSiO_3$ perovskites. *Physics and Chemistry of Minerals*, *25*, 515–521.

Sinogeikin, S., Bass, J., Prakapenka, V., Lakshtanov, D., Shen, G., Sanchez-Valle, C., & Rivers, M. (2006). Brillouin spectrometer interfaced with synchrotron radiation for simultaneous X-ray density and acoustic velocity measurements. *Review of Scientific Instruments*, *77*(10). https://doi.org/10.1063/1.2360884

Speziale, S., Marquardt, H., & Duffy, T. S. (2014). Brillouin scattering and its application in geosciences. *Reviews in Mineralogy and Geochemistry*, *78*(1), 543–603. https://doi.org/10.2138/rmg.2014.78.14

Stixrude, L., Lithgow-Bertelloni, C., Kiefer, B., & Fumagalli, P. (2007). Phase stability and shear softening in $CaSiO_3$ perovskite at high pressure. *Physical Review B: Condensed Matter and Materials Physics*, *75*(2), 24108.

Tappert, R., Stachel, T., Harris, J. W., Muehlenbachs, K., Ludwig, T., & Brey, G. P. (2005). Subducting oceanic crust: The source of deep diamonds. *Geology*, *33*(7), 565–568. https://doi.org/10.1130/g21637.1

Tauzin, B., Kim, S., & Afonso, J. C. (2018). Multiple phase changes in the mantle transition zone beneath northeast Asia: Constraints from teleseismic reflected and converted body waves. *Journal of Geophysical Research: Solid Earth*, *123*(8), 6636–6657. https://doi.org/10.1029/2017jb015238

Tauzin, B., Kim, S., & Kennett, B. (2017). Pervasive seismic low-velocity zones within stagnant plates in the mantle transition zone: Thermal or compositional origin? *Earth and Planetary Science Letters*, *477*, 1–13. https://doi.org/10.1016/j.epsl.2017.08.006

Thomson, A., Crichton, W., Brodholt, J., Wood, I., Siersch, N., Muir, J., et al. (2019). Seismic velocities of $CaSiO_3$ perovskite can explain LLSVPs in Earth's lower mantle. *Nature*, *572*(7771), 643–647. https://doi.org/10.1038/s41586-019-1483-x

Thomson, A., Crichton, W., Siersch, N., Ezad, I., Dobson, D., & Brodholt, J. (2025). Experimental observations of $CaSiO_3$-$CaTiO_3$ perovskites: Implications for Ca-rich inclusions observed in sub-lithospheric diamonds. *Physics and Chemistry of Minerals*, *52*(2), 19. https://doi.org/10.1007/s00269-025-01321-z

Tschauner, O., Huang, S., Yang, S., Humayun, M., Liu, W., Gilbert Corder, S. N., et al. (2021). Discovery of davemaoite, $CaSiO_3$-perovskite, as a mineral from the lower mantle. *Science*, *374*(6569), 891–894. https://doi.org/10.1126/science.abl8568

Walter, M. J., Bulanova, G., Armstrong, L. S., Keshav, S., Blundy, J. D., Gudfinnsson, G., et al. (2008). Primary carbonatite melt from deeply subducted oceanic crust. *Nature*, *454*(7204), 622–625. https://doi.org/10.1038/nature07132

Wang, X., Chen, Q.-F., Niu, F., Wei, S., Ning, J., Li, J., et al. (2020). Distinct slab interfaces imaged within the mantle transition zone. *Nature Geoscience*, *13*(12), 822–827. https://doi.org/10.1038/s41561-020-00653-5

Wei, W., Mao, Z., Sun, N., Sun, D., & Tkachev, S. N. (2021). High pressure-temperature single-crystal elasticity of grossular: Implications for the low-velocity layer in the bottom transition zone. *Geophysical Research Letters*, *48*(9), e2021GL093540. https://doi.org/10.1029/2021GL093540

Whitfield, C. H., Brody, E. M., & Bassett, W. A. (1976). Elastic moduli of NaCl by Brillouin scattering at high pressure in a diamond anvil cell. *Review of Scientific Instruments*, *47*(8), 942–947. https://doi.org/10.1063/1.1134778

Yu, Y., Zhang, X., Zhang, D., Li, L., Mao, Z., Sun, N., et al. (2025). Davemaoite elasticity reveals slab-induced heterogeneity in the Mantle transition zone [Dataset]. *Zenodo*. https://doi.org/10.5281/zenodo.18211476

Zhang, C., Yang, J.-Y., Sun, T., Zhang, H., & Brodholt, J. P. (2025). Strong precursor softening in cubic $CaSiO_3$ perovskite. *Proceedings of the National Academy of Sciences*, *122*(5), e2410910122. https://doi.org/10.1073/pnas.2410910122

References From the Supporting Information

Arimoto, T., Gréaux, S., Irifune, T., Zhou, C., & Higo, Y. (2015). Sound velocities of $Fe_3Al_2Si_3O_{12}$ almandine up to 19 GPa and 1700 K. *Physics of the Earth and Planetary Interiors*, *246*, 1–8. https://doi.org/10.1016/j.pepi.2015.06.004

Bass, J. D. (1989). Elasticity of grossular and spessartite garnets by Brillouin spectroscopy. *Journal of Geophysical Research*, *94*(B6), 7621–7628. https://doi.org/10.1029/jb094ib06p07621

Birch, F. (1947). Finite elastic strain of cubic crystals. *Physical Review*, *71*(11), 809–824. https://doi.org/10.1103/PhysRev.71.809

Birch, F. (1978). Finite strain isotherm and velocities for single-crystal and polycrystalline NaCl at high pressures and 300 K. *Journal of Geophysical Research*, *83*(B3), 1257–1268. https://doi.org/10.1029/jb083ib03p01257

Brown, J. M. (2018). Determination of elastic moduli from measured acoustic velocities. *Ultrasonics*, *90*, 23–31. https://doi.org/10.1016/j.ultras.2018.05.015

Chao, K.-H., Berrada, M., Wang, S., Peckenpaugh, J., Zhang, D., Chariton, S., et al. (2024). Structure and equation of state of Ti-bearing davemaoite: New insights into the chemical heterogeneity in the lower mantle. *American Mineralogist*, *109*(11), 1861–1870. https://doi.org/10.2138/am-2023-9104

Chen, G., Miletich, R., Mueller, K., & Spetzler, H. A. (1997). Shear and compressional mode measurements with GHz ultrasonic interferometry and velocity-composition systematics for the pyrope-almandine solid solution series. *Physics of the Earth and Planetary Interiors*, *99*(3–4), 273–287. https://doi.org/10.1016/s0031-9201(96)03205-0

Chen, H., Shim, S.-H., Leinenweber, K., Prakapenka, V., Meng, Y., & Prescher, C. (2018). Crystal structure of $CaSiO_3$ perovskite at 28–62 GPa and 300 K under quasi-hydrostatic stress conditions. *American Mineralogist*, *103*(3), 462–468. https://doi.org/10.2138/am-2018-6087

Conrad, P. G., Zha, C.-S., Mao, H.-K., & Hemley, R. J. (1999). The high-pressure, single-crystal elasticity of pyrope, grossular, and andradite. *American Mineralogist*, *84*(3), 374–383. https://doi.org/10.2138/am-1999-0321

Cottaar, S., Heister, T., Rose, I., & Unterborn, C. (2014). BurnMan: A lower mantle mineral physics toolkit. *Geochemistry, Geophysics, Geosystems*, *15*(4), 1164–1179. https://doi.org/10.1002/2013gc005122

Dolomanov, O. V., Bourhis, L. J., Gildea, R. J., Howard, J. A., & Puschmann, H. (2009). OLEX2: A complete structure solution, refinement and analysis program. *Applied Crystallography*, *42*(2), 339–341. https://doi.org/10.1107/s0021889808042726

Every, A. (1980). General closed-form expressions for acoustic waves in elastically anisotropic solids. *Physical Review B*, *22*(4), 1746–1760. https://doi.org/10.1103/physrevb.22.1746

Gréaux, S., Kono, Y., Wang, Y., Yamada, A., Zhou, C., Jing, Z., et al. (2016). Sound velocities of aluminum-bearing stishovite in the mantle transition zone. *Geophysical Research Letters*, *43*(9), 4239–4246. https://doi.org/10.1002/2016gl068377

Gwanmesia, G. D., Wang, L., Heady, A., & Liebermann, R. C. (2014). Elasticity and sound velocities of polycrystalline grossular garnet ($Ca_3Al_2Si_3O_{12}$) at simultaneous high pressures and high temperatures. *Physics of the Earth and Planetary Interiors*, *228*, 80–87. https://doi.org/10.1016/j.pepi.2013.09.010

Hill, R. (1952). The elastic behaviour of a crystalline aggregate. *Proceedings of the Physical Society Section A*, *65*(5), 349–354. https://doi.org/10.1088/0370-1298/65/5/307

Irifune, T., Higo, Y., Inoue, T., Kono, Y., Ohfuji, H., & Funakoshi, K. (2008). Sound velocities of majorite garnet and the composition of the mantle transition region. *Nature*, *451*(7180), 814–817. https://doi.org/10.1038/nature06551

Irifune, T., Sekine, T., Ringwood, A., & Hibberson, W. (1986). The eclogite-garnetite transformation at high pressure and some geophysical implications. *Earth and Planetary Science Letters*, *77*(2), 245–256. https://doi.org/10.1016/0012-821x(86)90165-2

Isaak, D. G., Anderson, O. L., & Oda, H. (1992). High-temperature thermal expansion and elasticity of calcium-rich garnets. *Physics and Chemistry of Minerals*, *19*(2), 106–120. https://doi.org/10.1007/bf00198608

Jiang, F., Gwanmesia, G. D., Dyuzheva, T. I., & Duffy, T. S. (2009). Elasticity of stishovite and acoustic mode softening under high pressure by Brillouin scattering. *Physics of the Earth and Planetary Interiors*, *172*(3–4), 235–240. https://doi.org/10.1016/j.pepi.2008.09.017

Kudo, Y., Hirose, K., Murakami, M., Asahara, Y., Ozawa, H., Ohishi, Y., & Hirao, N. (2012). Sound velocity measurements of $CaSiO_3$ perovskite to 133 GPa and implications for lowermost mantle seismic anomalies. *Earth and Planetary Science Letters*, *349*, 1–7. https://doi.org/10.1016/j.epsl.2012.06.040

Leitner, B. J., Weidner, D. J., & Liebermann, R. C. (1980). Elasticity of single crystal pyrope and implications for garnet solid solution series. *Physics of the Earth and Planetary Interiors*, *22*(2), 111–121. https://doi.org/10.1016/0031-9201(80)90052-7

Mao, Z., Fan, D., Lin, J.-F., Yang, J., Tkachev, S. N., Zhuravlev, K., & Prakapenka, V. B. (2015). Elasticity of single-crystal olivine at high pressures and temperatures. *Earth and Planetary Science Letters*, *426*, 204–215. https://doi.org/10.1016/j.epsl.2015.06.045

Milani, S., Angel, R. J., Scandolo, L., Mazzucchelli, M. L., Ballaran, T. B., Klemme, S., et al. (2017). Thermo-elastic behavior of grossular garnet at high pressures and temperatures. *American Mineralogist*, *102*(4), 851–859. https://doi.org/10.2138/am-2017-5855

Murakami, M., Sinogeikin, S. V., Litasov, K., Ohtani, E., & Bass, J. D. (2008). Single-crystal elasticity of iron-bearing majorite to 26 GPa: Implications for seismic velocity structure of the mantle transition zone. *Earth and Planetary Science Letters*, *274*(3–4), 339–345. https://doi.org/10.1016/j.epsl.2008.07.045

Nishihara, Y., Aoki, I., Takahashi, E., Matsukage, K. N., & Funakoshi, K.-i. (2005). Thermal equation of state of majorite with MORB composition. *Physics of the Earth and Planetary Interiors*, *148*(1), 73–84. https://doi.org/10.1016/j.pepi.2004.08.003

Noguchi, M., Komabayashi, T., Hirose, K., & Ohishi, Y. (2013). High-temperature compression experiments of $CaSiO_3$ perovskite to lowermost mantle conditions and its thermal equation of state. *Physics and Chemistry of Minerals*, *40*(1), 81–91. https://doi.org/10.1007/s00269-012-0549-1

O'Neill, B., Bass, J. D., Rossman, G. R., Geiger, C. A., & Langer, K. (1991). Elastic properties of pyrope. *Physics and Chemistry of Minerals*, *17*(7), 617–621. https://doi.org/10.1007/bf00203841

Ono, S., Ohishi, Y., & Mibe, K. (2004). Phase transition of Ca-perovskite and stability of Al-bearing Mg-perovskite in the lower mantle. *American Mineralogist*, *89*(10), 1480–1485. https://doi.org/10.2138/am-2004-1016

Pamato, M. G., Kurnosov, A., Ballaran, T. B., Frost, D. J., Ziberna, L., Giannini, M., et al. (2016). Single crystal elasticity of majoritic garnets: Stagnant slabs and thermal anomalies at the base of the transition zone. *Earth and Planetary Science Letters*, *451*, 114–124. https://doi.org/10.1016/j.epsl.2016.07.019

Sheldrick, G. M. (2008). A short history of SHELX. *Foundations of Crystallography*, *64*(1), 112–122. https://doi.org/10.1107/s0108767307043930

Shim, S. H., Duffy, T. S., & Shen, G. (2000). The stability and P–V–T equation of state of $CaSiO_3$ perovskite in the Earth's lower mantle. *Journal of Geophysical Research*, *105*(B11), 25955–25968.

Shim, S. H., Jeanloz, R., & Duffy, T. S. (2002). Tetragonal structure of $CaSiO_3$ perovskite above 20 GPa. *Geophysical Research Letters*, *29*(24), 19-11–19-14. https://doi.org/10.1029/2002gl016148

Sinogeikin, S. V., & Bass, J. D. (2000). Single-crystal elasticity of pyrope and MgO to 20 GPa by Brillouin scattering in the diamond cell. *Physics of the Earth and Planetary Interiors*, *120*(1–2), 43–62. https://doi.org/10.1016/s0031-9201(00)00143-6

Sinogeikin, S. V., & Bass, J. D. (2002a). Elasticity of Majorite and a majorite-pyrope solid solution to high pressure: Implications for the transition zone. *Geophysical Research Letters*, *29*(2), 4-1–4-4. https://doi.org/10.1029/2001gl013937

Sinogeikin, S. V., & Bass, J. D. (2002b). Elasticity of pyrope and majorite–pyrope solid solutions to high temperatures. *Earth and Planetary Science Letters*, *203*(1), 549–555. https://doi.org/10.1016/s0012-821x(02)00851-8

Sinogeikin, S. V., Bass, J. D., & Katsura, T. (2003). Single-crystal elasticity of ringwoodite to high pressures and high temperatures: Implications for 520 km seismic discontinuity. *Physics of the Earth and Planetary Interiors*, *136*(1–2), 41–66. https://doi.org/10.1016/s0031-9201(03)00022-0

Speziale, S., & Duffy, T. S. (2002). Single-crystal elastic constants of fluorite (CaF_2) to 9.3 GPa. *Physics and Chemistry of Minerals*, *29*(7), 465–472. https://doi.org/10.1007/s00269-002-0250-x

Stixrude, L., & Lithgow-Bertelloni, C. (2005). Thermodynamics of mantle minerals - I. Physical properties. *Geophysical Journal International*, *162*(2), 610–632. https://doi.org/10.1111/j.1365-246X.2005.02642.x

Sun, N., Bian, H., Zhang, Y., Lin, J.-F., Prakapenka, V. B., & Mao, Z. (2022). High-pressure experimental study of tetragonal $CaSiO_3$-perovskite to 200 GPa. *American Mineralogist: Journal of Earth and Planetary Materials*, *107*(1), 110–115. https://doi.org/10.2138/am-2021-7913

Sun, N., Mao, Z., Yan, S., Wu, X., Prakapenka, V. B., & Lin, J. F. (2016). Confirming a pyrolitic lower mantle using self-consistent pressure scales and new constraints on $CaSiO_3$ perovskite. *Journal of Geophysical Research: Solid Earth*, *121*(7), 4876–4894. https://doi.org/10.1002/2016jb013062

Wang, Y., Weidner, D. J., & Guyot, F. (1996). Thermal equation of state of $CaSiO_3$ perovskite. *Journal of Geophysical Research*, *101*(B1), 661–672.

Zhang, Y., Fu, S., Wang, B., & Lin, J.-F. (2021). Elasticity of a pseudoproper ferroelastic transition from stishovite to post-stishovite at high pressure. *Physical Review Letters*, *126*(2), 025701. https://doi.org/10.1103/physrevlett.126.025701

Zhou, C., Gréaux, S., Liu, Z., Higo, Y., Arimoto, T., & Irifune, T. (2021). Sound velocity of $MgSiO_3$ majorite garnet up to 18 GPa and 2000 K. *Geophysical Research Letters*, *48*(14), e2021GL093499. https://doi.org/10.1029/2021gl093499

Erratum

The originally published version of this article contained an error in Table S4. The V_P and V_S values reported in the table were inadvertently calculated using the G_V. The values should have been calculated using G, defined as the average of G_V and G_R, as described in Text S3 in the supporting information. The errors have been corrected, and this may be considered the authoritative version of record.